

SPECTROSCOPIC SUBSYSTEMS IN NEARBY WIDE BINARIES

ANDREI TOKOVININ

Cerro Tololo Inter-American Observatory, Casilla 603, La Serena, Chile
Draft version July 18, 2018

ABSTRACT

Radial velocity (RV) monitoring of solar-type visual binaries has been conducted at the CTIO/SMARTS 1.5-m telescope to study short-period systems. Data reduction is described, mean and individual RVs of 163 observed objects are given. New spectroscopic binaries are discovered or suspected in 17 objects, for some of them orbital periods could be determined. Subsystems are efficiently detected even in a single observation by double lines and/or by the RV difference between the components of visual binaries. The potential of this detection technique is quantified by simulation and used for statistical assessment of 96 wide binaries within 67 pc. It is found that 43 binaries contain at least one subsystem and the occurrence of subsystems is equally probable in either primary or secondary components. The frequency of subsystems and their periods match the simple prescription proposed by the author (2014, AJ, 147, 87). The remaining 53 simple wide binaries with a median projected separation of 1300 AU have the distribution of the RV difference between their components that is not compatible with the thermal eccentricity distribution $f(e) = 2e$ but rather matches the uniform eccentricity distribution.

Subject headings: stars: binaries

1. INTRODUCTION

Binary and multiple systems are ubiquitous products of star formation (Duchêne & Kraus 2013). The gas condensing into stars contains excessive angular momentum that is transported outwards during collapse and accretion and stored partially in the orbital momentum of binaries. While the basic physics is known, no current theory is able to predict the multiplicity fraction and the distributions of separations, mass ratios, or eccentricities, although large-scale numerical simulations show promising agreement with observations (Bate 2012). Formation of binary stars is related to the stellar mass function and sets the scene for subsequent evolution (mass transfer, blue stragglers, X-ray binaries, and type I supernovae). On the other hand, the gas left around newly born stars as a material for planet formation is inherited from the epoch of mass accretion and is related to multiplicity. The common origin of stars, planets, and binaries should therefore be studied jointly.

Solid observational data on binary statistics are difficult to get because of various selection effects, and this is exacerbated for stellar hierarchies containing three or more stars. Yet, hierarchical multiple systems give additional insights into star formation from their period ratios, relative orbit orientation, and structure. This work complements the study of hierarchical multiplicity of solar-type stars in the 67-pc volume (Tokovinin 2014a,b, hereafter FG67a and FG67b). The large size of the FG-67 sample defined in FG67a (4867 stars) and modest and well-controlled observational selection allowed reliable estimates of the fraction of hierarchical systems, 13%, and of their statistics. One unexpected result was the large fraction of subsystems in the secondary components of wide binaries and the emerging correlation between subsystems, so that 4% of targets turned out to be 2+2 quadruples (two close binaries on a wide

orbit around each other). However, this result relied on extrapolation from the small number of well-studied secondary components. While the main targets of the FG-67 sample were the subject of spectroscopic and imaging observational campaigns, the secondaries were generally neglected. Recent imaging studies of secondary components (Riddle et al. 2015; Tokovinin 2014c) have largely remedied the situation, but *close* secondary subsystems accessible only to spectroscopy still remain to be discovered. Exploring these close subsystems is the main motivation of the present work.

I report here RV monitoring of solar-type stars in the FG-67 sample that are either known to be spectroscopic binaries but lack the orbit or belong to wide visual binaries. Most targets have southern declinations. The main goal is characterization of subsystems in the secondary components and determination of their periods, complementing previous efforts in this respect. Extensive previous RV data were furnished by the Geneva-Copenhagen Survey, GCS (Nordström et al. 2004), which covered mostly the main targets. As a continuation of this campaign, Halbwachs et al. (2012) monitored the RVs of wide pairs, discovering several subsystems. Tokovinin & Smekhov (2002) reported RV monitoring of both wide and close (unresolved on the slit) visual binaries, mostly on the northern sky. A similar, but much smaller survey of southern multiples is published by Tokovinin et al. (2015a). Desidera et al. (2006) measured precise RVs of wide binaries in search of stellar or planetary subsystems. These survey-type works are complemented by studies of individual objects published by various authors Griffin (e.g. 2001). Although this paper is devoted to wide binaries, RVs of all observed stars are given. Presentation of newly determined orbits is deferred to a future paper, as their lengthy discussion would distract from the main topic, while binaries needing more data are still being observed.

The instruments, data reduction, and raw results are

covered in Section 2. Then in Section 3 I evaluate through simulation the proposed method of detecting subsystems from a single observation. Section 4 reports on subsystems in a volume-limited sample of wide binaries. In Section 5 the RV difference in wide binaries without subsystems is analyzed to constrain their eccentricities. The work is summarized in Section 6.

2. OBSERVATIONS AND RESULTS

2.1. Observing campaigns and instruments

The observations reported in this paper were obtained with the 1.5-m telescope located at the Cerro Tololo Interamerican Observatory in Chile and operated by the SMARTS Consortium.¹ The observing time was allocated through NOAO (programs 10B-0022, 14B-0009, and 15A-0055). The observations were made by the telescope operators in service mode.

The goal of the 2010 campaign was to determine unknown spectroscopic orbits of close solar-type binaries and to observe components of wide binaries that lacked RV coverage. At least three observations of each target were planned in the 20 allocated nights. However, less time was actually scheduled, so most targets were observed just once, and only a few were pointed several times. This data set is therefore too small for addressing the goals of the original proposal. Nevertheless, one orbit was determined and several subsystems were discovered.

In 2010, the spectra were taken with the Fiber Echelle (FECH) instrument. It was the de-commissioned echelle spectrometer from the Blanco 4-m telescope moved to the Coudé room of the 1.5-m telescope and fed by the fiber. In this program the image of the fiber projected into the spectrograph was not masked by the slit and its width defined the spectral resolution of $R = 44\,000$. The detector was a SIT CCD of 2014×2048 pixels format with the Arcon controller. The calibration spectrum of the thorium-argon lamp fed through the same fiber was taken before or after each target.

In 2014 and 2015, observations were made with the CHIRON spectrograph (Tokovinin et al. 2013) that replaced FECH in 2011. Stars brighter than $V \sim 9.5$ mag were observed in the slicer mode with a spectral resolution of $R = 90\,000$, while for fainter targets the fiber mode with $R = 28\,000$ was used. When both components of a wide binary were observed, the same mode was chosen. The thorium-argon calibrations were recorded for each target.

The observing campaigns of 2014 and 2015 targeted secondary components of wide binaries in a “snapshot survey” designed to detect subsystems from just one observation by RV difference between the components. I selected binaries from the FG-67 sample south of $+20^\circ$ declination with separations no less than $8''$ to ensure that the components are well resolved on the entrance fiber aperture. Only the secondaries with V magnitudes between 8 and 11 were chosen to shorten the exposure time, maximizing the sample coverage. Secondaries with prior RV coverage were removed from the program; however, they are included in the statistical analysis in Section 4. Primary components were observed as well if they lacked prior RV data comparable in quality to the GCS

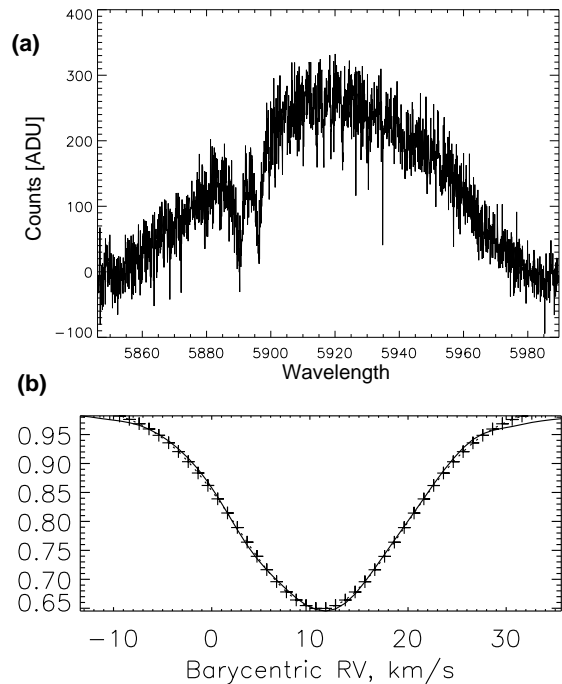


Figure 1. Example of FECH data. The top plot (a) shows the extracted echelle order in the region of sodium D lines. The spectrum of the $V = 10.5^m$ star HIP 9902B was taken on JD 2455449 with a 10-min. exposure. The lower plot (b) shows the CCF of this spectrum with the solar mask (line) and its Gaussian fit (crosses; RV 11.12 km s^{-1} , amplitude 0.351, dispersion 8.42 km s^{-1}). The rms deviation from the fit is 0.007.

(two or three observations with a time base of at least a year). Also, monitoring of several known solar-type spectroscopic binaries was continued for computing their orbits.

2.2. Data reduction

The reduced and wavelength-calibrated spectra delivered by the CHIRON pipeline were retrieved from the SMARTS center at the Yale University. The availability of this service has greatly enhanced this program by allowing rapid analysis of the RVs and flexible scheduling of new observations when needed.

The FECH data were reduced by the author using a simplified and adapted version of the CHIRON pipeline software (Tokovinin et al. 2013). I extracted echelle orders 84 to 123 covering the wavelength range from 4500 \AA to 6850 \AA . At shorter wavelengths, there is little signal in the spectra of red stars and quartz lamp, while longer wavelengths are affected by telluric absorptions and are not used in the cross-correlation. A set of 10 quartz spectra was co-added and used to extract the stellar and arc spectra in a boxcar window of ± 8 pixels. The position of the spectra on the CCD, defined by the fiber, was stable to within 0.5 pixels. Cosmic rays were removed during the order extraction, but the current algorithm did not detect all these events and some spectra do contain a few residual spikes.

While the extracted CHIRON spectra are corrected for small-scale variations of the detector sensitivity using the quartz lamp calibration, this correction was not applied to the FECH data because the quartz “flats” for FECH deviate from unity by only a few percent, less than the typical noise. The FECH wavelength calibration typ-

¹ <http://www.astro.yale.edu/smarts/>

ically used 1400 thorium-argon lines with a scatter of 0.1 pixels or 0.36 km s^{-1} between the measured line positions and their 6-th order polynomial approximation. Each science spectrum was paired with the wavelength calibration closest in time (typically within 3 minutes).

2.3. Radial velocities by cross-correlation

The spectra were cross-correlated with the digital binary mask based on the solar spectrum stored in the NOAO archive (see Tokovinin et al. 2015a, for more details). Figure 1 shows data on a faint target. The extracted FECH spectrum has ~ 250 counts (the gain is 1.4 el/ADU). However, the cross-correlation function (CCF) is very smooth. Its Gaussian fit leads to $RV = 11.114 \pm 0.067 \text{ km s}^{-1}$. The amplitude of the Gaussian is $a = 0.351 \pm 0.002$ and its dispersion is $\sigma = 8.415 \pm 0.16 \text{ km s}^{-1}$. The rms residual to the fit is 0.7%. The RVs are derived without applying any zero-point correction from RV standards, they are tied directly to the solar spectrum.

The CCF $C(v)$ is computed over the RV range of $v = \pm 200 \text{ km s}^{-1}$. A Gaussian is fitted to the portion of the CCF within $\pm 2.35\sigma$ of the minimum. When two or three Gaussians are fitted, the data around all the minima are used jointly. After the first iteration, the centers and dispersions are determined, and in the second iteration the fitting area is adjusted accordingly. The CCF model with k Gaussians is

$$C(v) = 1 - \sum_{j=1}^k a_j \exp[-(v - v_j)^2 / 2\sigma_j^2] \quad (1)$$

and contains $3k$ free parameters (v_j, a_j, σ_j). It is possible to fix some parameters, but this option, handy for deblending overlapping CCFs, was not used in the data reported below.

Formal errors of the fitted parameters do not reflect their real precision, being dominated by systematic, rather than random, deviations of the CCF from its model. I do not provide these errors in the data table. The real RV precision estimated from residuals to orbital fits is about 0.1 km s^{-1} for both CHIRON and FECH. For example, 4 observations of HIP 105585C taken with CHIRON over a time span of 333 days have rms scatter of 40 m s^{-1} . The bright star HIP 5896 with a very wide CCF ($\sigma = 33 \text{ km s}^{-1}$) observed 11 times with FECH shows the rms RV scatter of 0.28 km s^{-1} .

For 21 apparently single stars the RVs were measured both here and in the GCS. The average difference CHIRON–GCS is 0.47 or 0.36 km s^{-1} (with or without rejecting one outlier, respectively). The rms scatter of the difference is 0.58 km s^{-1} . This minor systematics is ignored in the following, being most likely attributable to the CORAVEL instruments used by the GCS. More accurate RVs (Nidever et al. 2002; Desidera et al. 2006) match the CHIRON data better.

2.4. Data tables

Table 1 lists all 163 observed targets. Column (1) identifies the target by the *Hipparcos* number of the main component and, where necessary, the component letter. As most (but not all) targets belong to the FG-67 sample, additional information such as equatorial coordinates,

proper motions, and magnitudes in various pass-bands can be retrieved from the FG67a paper. The following columns list the average RV, the number of observations, and the tag that combines the maximum number of fitted Gaussians (e.g. 2 for a double-lined binary) with the instrument code, C for CHIRON and F for FECH. Asterisk after the tag signals a spectroscopic system discovered in this survey, the letter O means that spectroscopic orbit has been computed.

Table 2, published in full electronically, gives individual observations. Its column (1) contains the target name (as in Table 1). Columns (2) to (5) contain the heliocentric Julian date and the parameters (v, a, σ) from the Gaussian fits (equation 1). If more than one component was fitted, the parameters of additional components are listed separately, with the same date. The last column (6) contains a tag that combines the number j of the fitted Gaussian with the instrument code. The Table contains 343 individual observations, 233 made with FECH and 110 with CHIRON.

Short comments on new spectroscopic systems or other objects for which the new data are interesting in some or other way are assembled in Table 3. Asterisks mark 17 systems or subsystems discovered in this survey. Orbital periods are given here for reference only, pending publication of the full analysis. Some stars with asymmetric CCFs, presumably binaries with components of comparable luminosity and small RV difference, were resolved recently by speckle interferometry at the SOAR telescope (Tokovinin et al. 2015b).

3. DETECTION OF SUBSYSTEMS FROM RV DIFFERENCE BETWEEN BINARY COMPONENTS

Subsystems with large mass ratios are readily detected by the appearance of double or blended lines in a single spectrum. When the visual orbit is known, the RV difference for the moment of observation can be computed using estimated masses. If the observed RV difference is discrepant even after re-adjusting the visual orbit, the presence of a subsystem in one of the components is strongly suspected. This is the case of HIP 105947, 109951, and 117666.

The alternative idea of detecting subsystems in wide binaries from the RV difference between the components (as in HIP 12780, 14519, 76435) is explored here by means of simulation. We need to decide whether the wide binary contains a subsystem (hypothesis H1) or is just a binary (hypothesis H0), based on a single measurement of the RV difference between its components $\Delta V = |V_1 - V_2|$. The quantity ΔV is measured with some error. Moreover, the wide binary is itself in orbital motion, so the RVs of its components are not exactly equal even without subsystems.

First, I establish the distribution of the orbital RVs of spectroscopic binaries. The RV semi-amplitude K_1 depends on the orbital inclination i and eccentricity e as

$$K_1 = A_1 \sin i (1 - e^2)^{-1/2},$$

$$A_1 = 29.8 P^{-1/3} M_2 (M_1 + M_2)^{-2/3}. \quad (2)$$

Here A_1 (the RV semi-amplitude in a circular orbit at $i = 90^\circ$, in km s^{-1}) is related to the orbital period P (in years) and the component masses M_1 and M_2 (in solar-

Table 1
Summary of observations

HIP	RV km s ⁻¹	<i>N</i>	Tag	HIP	RV km s ⁻¹	<i>N</i>	Tag	HIP	RV km s ⁻¹	<i>N</i>	Tag
5896	7.79	10	1F	37645B	-16.39	1	1C	98274	-19.31	1	1F
6772A	49.87	1	1C	38908B	16.98	1	1F	99572	27.27	1	1F
6772B	50.43	1	1C	40452B	21.19	1	1F	99651A	24.27	2	1F
7601	-10.61	12	3CO	41353A	7.31	2	1F	100895	-14.97	1	1F
8486B	-6.65	1	1F	41353B	28.51	3	2F*	100896	-5.81	11	2F
9497	17.81	1	1F	44579B	0.60	1	1F	101443	23.03	1	1F
9642	44.90	10	2CO	45734B	-7.78	3	2F	101551B	21.38	2	1F
9902A	11.48	2	1F	45734A	0.14	2	2F	101551A	21.41	2	1C
9902B	11.03	2	1F	45838A	54.95	1	1F	102418C	11.34	1	1C
9911B	-38.69	2	1F	46236B	30.95	2	1F	102655B	-2.34	1	1C
9911A	-39.13	1	1F	47862B	-14.46	1	1F	102655A	-2.64	1	1C
10579B	44.28	1	1F	49030B	15.83	1	1F	102945	-22.12	1	1F
10579A	38.94	1	1F	59272B	2.74	1	1F	103578	-31.01	1	1F
10754	44.82	2	1C	59690B	25.10	2	1F	104687B	-21.17	1	1F
11024A	45.19	1	1F	60353B	4.35	1	1F	104687A	-20.47	1	1F
11024B	45.19	2	1F	60749D	-1.77	1	1F	105569	-1.97	1	2F
11324A	34.35	1	1F	61595B	-15.33	1	1F	105569C	3.79	1	1F
11324B	32.90	1	1F	64478A	-40.23	10	3FO	105585C	3.63	4	1C
11417	62.92	1	2F	64478B	20.03	22	2F*O	105585A	-1.80	4	2C
11537	30.23	4	2F*	64498B	-15.73	1	1F	105879D	35.90	2	1F
11783B	-28.26	1	1C	64498A	-12.04	1	1F	105879A	40.17	3	2F*O
11783A	-24.58	1	1C	66121B	-28.41	1	1F	105947	22.13	1	2F*
11909	6.14	1	1F	66676A	1.40	2	1F	106438A	-29.24	1	1F
12326A	17.00	1	1F*	66676B	2.37	1	1F	106438B	-28.99	1	1C
12326B	19.21	1	1F	67246B	-30.37	1	1F	106632A	16.73	1	1C
12361	19.36	1	1F	67408B	2.89	1	1F	106632B	16.31	1	1C
12764A	14.75	2	1F	69220B	49.95	1	1F	107299	37.31	1	1F
12780B	-3.44	9	1F*O	71682C	13.22	2	1F	107300	37.31	1	1F
12780A	-6.64	7	2FO	72235A	9.13	1	1F	109035C	-14.62	1	1F
12884	43.78	1	1F	72235B	9.08	1	1F	109035B	4.74	1	1F
13498	13.88	8	3CO	74975B	55.08	1	1F	109035A	-8.67	1	1F
13725	10.28	1	1F	76435C	7.34	2	1F*	109951	-24.04	1	2F*
14194A	35.32	1	1C	76435A	5.47	3	1F	110091	16.05	1	1F
14194B	31.86	3	2C*	76888A	8.06	1	1F	110447A	2.47	1	1C
14307B	19.89	3	2C*	76888B	7.90	1	1F	110447B	1.37	1	1C
14519B	17.70	2	1C	79730B	-40.08	1	1C	110712A	14.57	1	1F
14519A	15.87	2	1C*	83701B	-1.09	1	1C	110712B	15.28	1	1F
16860B	-24.93	1	1C	85342B	-15.85	1	1C	111903	41.68	1	1F*
22611B	46.03	1	1C	87813B	-5.94	3	1C	112201B	-12.87	1	1C
22611A	45.72	1	1C	89805B	1.61	1	1F	112325	-28.07	1	1F
22611C	46.39	1	1C	89805A	0.87	1	1F	113386A	0.46	1	1F
22683B	4.71	1	1C	89808	8.14	1	1F	113386B	0.85	2	1F
22693B	-0.65	1	1C	91837C	-3.65	1	1F	113579	7.03	1	1F
23926B	45.09	1	1F	91837A	-3.58	1	1F	113597	20.55	5	3F*
24711B	-10.79	1	1C	92140	4.60	9	1F	114167B	4.81	1	1F
25082B	23.23	1	1F	94310	-15.12	1	1F	114167A	4.25	1	1F
27922B	44.03	1	1F	94389	23.49	1	1F	115087	15.21	10	1FO
28790B	34.92	10	2C*O	95106A	9.35	2	1F	116063B	4.30	1	1F
28790A	17.20	8	1CO	95106B	9.29	5	1F*	116063A	4.03	1	1F
31711C	31.58	1	1C	95116B	-41.12	3	1C	117081A	21.79	1	1F
35261C	23.83	3	2C	95116A	-41.93	1	1C	117081B	21.24	1	1F
36165B	64.86	1	1C	95847	-23.95	1	1F	117391B	17.74	1	1C
36165A	66.23	1	1C	97508C	8.04	2	1F	117666	9.82	1	2F*
36640B	56.25	1	1C	97508A	8.32	1	1F				
37645A	-19.52	1	1C	97548	-8.46	1	1F				

Table 2
Individual radial velocities (fragment)

HIP, Comp.	HJD +24 00000	RV km s ⁻¹	<i>a</i>	σ km s ⁻¹	Tag
5896	55490.6235	7.784	0.040	33.504	1F
5896	55510.5567	7.880	0.040	33.680	1F
6772A	56863.8045	49.866	0.201	5.638	1C
6772B	56863.7976	50.427	0.280	6.495	1C
8486B	55436.9363	-6.649	0.299	4.973	1F
9497	55436.9452	17.811	0.223	5.318	1F
9902A	55449.8915	11.836	0.072	18.887	1F

mass units). The coefficient 29.8 km s⁻¹ is the average

orbital velocity of the Earth.

A large number ($N = 10\,000$) of spectroscopic binaries was simulated. Their RV V_1 was calculated at random orbital phase. The influence of masses and periods is eliminated by studying the distribution of dimensionless quantity $x = |V_1|/A_1$. Only the random effects of inclination, eccentricity, and phase remain. I assume isotropic orbit orientation which corresponds to the uniform distribution of $\cos i$. The distribution of x depends on the distribution of orbital eccentricity. Four cases are considered: (1) $e = 0$ (circular orbits), (2) sine distribution $f(e) = \pi/2 \sin(\pi e)$, (3) uniform distribution $f(e) = 1$, and (4) linear distribution $f(e) = 2e$, often called ‘‘ther-

Table 3
Comments on individual objects

HIP	Comment
6896	F6IV star belongs to the nearby (20 pc) visual quadruple system κ Tuc. The RV is 1.1 km s^{-1} and variable (GCS), 7.8 km s^{-1} and constant here. <i>Hipparcos</i> acceleration. Orbital period of several years?
7601	SB3, two orbits and speckle resolution, periods 19.4 and 614 days.
9497	Close visual triple system without prior RV data. The CCF has only one narrow dip.
9642	SB2 discovered in GCS, orbit $P = 4.78 \text{ d}$.
10579	Algol-type eclipsing binary DS Cet, but the CCFs of A and B are narrow.
10754	The component A = HIP 10621 at $836''$ is optical, different RV.
11417	SB2 discovered by D. Latham (2012, private communication); here double-lined with equal components.
11537	* New SB2, <i>Hipparcos</i> acceleration. Possibly resolvable by speckle interferometry.
11783	A was resolved at SOAR at $0''.2$, which explains its RV difference with B.
12326	* A has asymmetric CCF, RV differs from B and C. Possibly resolvable by speckle.
12780	* B is new SB1, orbit $P = 27.8 \text{ d}$. A is SB2 and visual binary.
12884	Eclipsing binary CN Hyi in a 78-year visual binary. The RV here refers to the visual secondary with narrow CCF. Two wide, low-contrast dips of the eclipsing pair are also present in the CCF, but they were not measured.
13498	SB3 discovered by Tokovinin et al. (2015a), orbit with $P = 13.75 \text{ d}$, correction of the visual orbit.
14194	* B is new SB2 with a period on the order of a year.
14307	* B has asymmetric CCF. It was resolved at SOAR at $0''.19$, estimated period 25 yr.
14519	* RV difference of 1.8 km s^{-1} between A and B indicates a subsystem in one of the components.
22683	The B-component HIP 22668 at $796''$ has different RV, it is either optical or contains a subsystem.
26611	Three components at $100''$ and $52''$ in non-hierarchical configuration have matching RVs.
28790	* Orbits for A ($P = 221 \text{ d}$) and B (new SB2, $P = 13.23 \text{ d}$).
35261	C is an SB2 discovered by Tokovinin et al. (2015a).
37645	A is a known SB resolved at SOAR at $0''.20$, hence the RV difference with B.
41353	* B=HD 71842 is a new SB2, at $297''$ from A, optical. For this reason orbit determination is not attempted.
45734	Young quadruple: A is a close pair, while B has double lines (Desidera et al. 2006). The CCFs of B are of strange rectangular shape, possibly triple-lined, while the CCF of A is asymmetric.
64478	* B is a new SB2, orbit $P = 0.24 \text{ d}$. Updated orbit of A, $P = 4.3 \text{ d}$
66676	B is a triple system resolved at SOAR, but its CCF is narrow, while the RVs of A and B match.
72235	B was resolved at SOAR at $0''.4$, but its CCF is narrow, while the RV matches that of A.
76435	* RV(C) differs from RV(A). C was resolved at SOAR at 56 mas , estimated period 4 yr.
85342	B = HIP 85326 is a spectroscopic and acceleration binary resolved at SOAR.
87813	B is a spectroscopic binary discovered by Tokovinin & Smekhov (2002).
92140	SB1 with slow RV variation (FECH, also N. Gorynya, private communication, 2013).
95106	* B = HIP 95110 is a new SB1 with period of a few months. A was resolved at SOAR at $0''.27$.
95116	HIP 96979 has matching RV, similar proper motions and parallaxes. Too distant to be a bound binary, however.
95708	AB is a 65-year visual binary, its CCF is asymmetric. The RV(C) is similar, physical triple.
98274	Close visual binary, its CCF is asymmetric. This is the first RV measurement.
100896	The RVs match the 160-day SB2 orbit by Halbwachs et al. (2012), B = HIP 100895 is physical.
102945	Fast axial rotation ($\sigma = 20.2 \text{ km s}^{-1}$); it is a $0''.8$ visual binary with evolved component.
105585	AB is a visual binary I 337, seen as SB2 here. All data can be fitted by a 207-year orbit with $e = 0.72$.
105879	* A is SB2, preliminary orbit with $P = 9 \text{ yr}$, also <i>Hipparcos</i> acceleration.
105947	* SB2 and 20.7-year visual binary with a well-defined orbit. $\Delta V = 17 \text{ km s}^{-1}$ is 2.2 times larger than predicted, caused by a subsystem?
109951	* Double CCF, suspected subsystem in the secondary component. $\Delta V = 12.5 \text{ km s}^{-1}$ is 3 times larger than predicted by the visual orbit.
110091	Close visual binary CHR 107 with estimated period of ~ 6 years. The CCF is slightly asymmetric.
110792	B=HIP 110719 at $20''.6$ was resolved at SOAR at $0''.19$, explaining the RV difference.
111903	* RV(A) differs by 3.4 km s^{-1} from the RV reported in GCS, hence new SB?
113597	* New SB3. It is a $1''.8$ visual binary, while HIP 113579 at $581''$ also belongs to the system.
115087	SB1 discovered by GCS, orbit $P = 7.88 \text{ d}$.
117666	* The 30-year visual orbit of A 2700 predicts ΔV of 2.7 km s^{-1} , here $\Delta V = 16.3 \text{ km s}^{-1}$, hence a subsystem.

mal". In the additional case 2a, the eccentricity of case 2 is multiplied by 0.7 to get the average $e = 0.35$ typical of spectroscopic binaries.

Figure 2 shows the results. In the case (1), the strict inequality $K_1 \leq A_1$ holds. Combination of random phase and random inclination results in the uniform distribution of x in the interval $[0, 1]$, so its cumulative distribution is linear, $F(x) = x$. Larger RV variations are produced in eccentric orbits. Their probability is small, increasing with the increasing fraction of eccentric orbits. On the other hand, the median of the RV distribution depends on the eccentricity much less.

A spectroscopic binary can be detected by a large RV variation. The probability of such event $p_{\text{det}}(x) = 1 - F(x)$ is defined by the cumulative distribution $F(x)$. I

found a good analytical approximation for the case 2,

$$p_{\text{det}}(x) = 1 - F(x) \approx 10^{-x[0.65 - 0.32/(1+4x^3)]} \quad (3)$$

(crosses in Figure 2). If the eccentricity is distributed uniformly (case 3), the formula (3) is still good at small x .

The observed RV difference ΔV includes a contribution from the orbital motion in wide binary. A subsystem is detectable from a single observation when ΔV significantly exceeds the orbital velocity of the outer binary. The latter is estimated statistically using simulations. The relevant normalization factor is now

$$A_L = 29.8 P_L^{-1/3} M_L^{1/3} \quad (4)$$

instead of A_1 . I denote the "long" period of the wide binary by P_L , its mass sum by M_L , and the correspond-

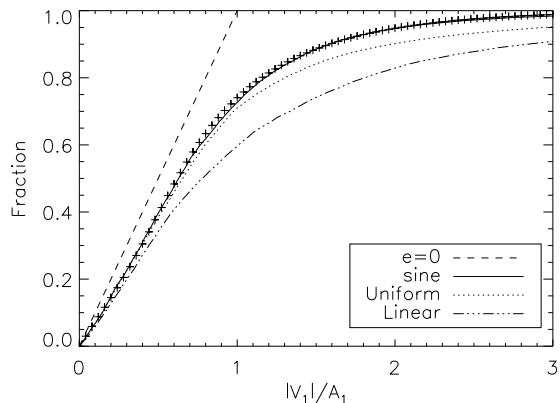


Figure 2. Cumulative distributions of normalized orbital velocities $x = |V_1|/A_1$ for different eccentricity distributions of spectroscopic binaries. The plus signs correspond to the analytical approximation.

ing amplitude of the RV difference by A_L . For the long period of 10^3 years and a mass sum of $1 M_\odot$, the amplitude is 0.1 of the Earth speed or 3 km s^{-1} . Considering that the errors of RVs measured with CHIRON are on the order of 0.1 km s^{-1} , it is clear that the RV difference is dominated by the motion in wide binaries, while the measurement errors are negligible in comparison.

In the case of wide binaries, we do not know their true orbital periods P_L and estimate them by assuming that projected separation equals semi-major axis a_L . Considering that $P_L \propto a_L^{3/2}$, the estimated amplitude becomes $A^* = A_L(a_L/\rho)^{0.5}$. This has been accounted for in the simulations. Normalized RV amplitudes using projected separations (A^* instead of A_L) are slightly smaller because, statistically, A^* is larger than A_L . Cumulative distributions for different cases are plotted in Figure 3.

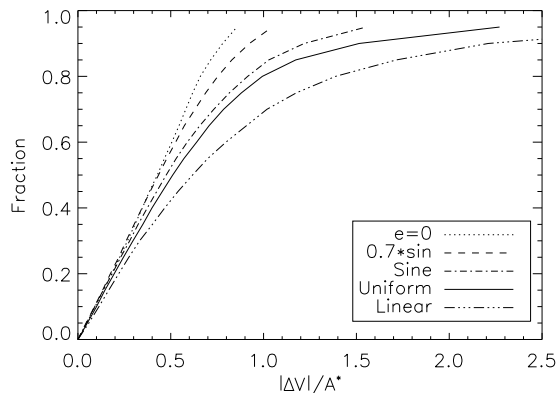


Figure 3. Cumulative distributions of normalized orbital RV difference $F(|\Delta V|/A^*)$ for wide binaries with various eccentricity distributions.

The probability that the measured RV difference ΔV is compatible with the hypothesis H0 (no subsystems) is estimated through cumulative distribution $F(|\Delta V|/A^*)$ as

$$p(\text{H0}) = 1 - F(|\Delta V|/A^*). \quad (5)$$

Let ϵ be a small number characterizing the false alarm probability (detection of a non-existent subsystem). The hypothesis H0 is rejected if $p(\text{H0}) < \epsilon$, or $F(|\Delta V|/A^*) > 1 - \epsilon$. Adopting $\epsilon = 0.05$, the detection limit for subsystems translates to $x > k_L(\epsilon)$, where $k_L = 0.85$ for

circular outer orbits, $k_L = 1.55$ for the sine eccentricity distribution, and $k_L = 2.40$ for the uniform distribution of eccentricity in the outer orbits.

Now the tools are in place to estimate the probability of detecting a subsystem in a wide binary from a single measurement of ΔV . For each combination of the mass ratio q_S and period P_S in the subsystem, the amplitude A_1 is computed by (2). The detection threshold is $V_1 > k_L A_L^*$ or $x > k_L A_L^*/A_1$. The probability of such event is estimated by the approximate formula (3). A single measurement of ΔV provides thus statistical constraints on the presence of subsystems in both components of a wide binary. This reasoning does not apply to wide binaries with known subsystems, e.g. containing close inner visual binaries, where ΔV is likely produced by motion in those subsystems, rather than in the wide binary itself.

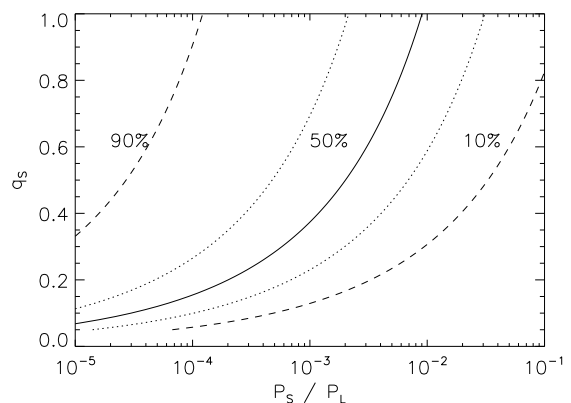


Figure 4. Probability of detecting a subsystem by the RV difference method as a function of the period ratio P_S/P_L and mass ratio in the subsystem q_S . The curves, left to right, depict the detection probability of 90%, 70%, 50% (full line), 30%, and 10%.

Period ratio vs. mass ratio in detectable subsystems is plotted in Figure 4 with the following assumptions: $M_L = 2M_1$, sine eccentricity distribution in inner subsystems, and $k_L = 2.4$. Note the “fuzzy” character of this detection technique: the chance to miss a subsystem is substantial for all parameters. This is the penalty for using just a single RV measurement. The detection curves are described by

$$\frac{q_S}{(1 + q_S)^{2/3}} > \frac{k_L}{x(p_{\text{det}})} (2P_S/P_L)^{1/3}, \quad (6)$$

where $x(p_{\text{det}})$ is determined by inverting (3), namely 0.15, 0.39, 0.63, 0.95, and 1.60 for probabilities of 0.1, 0.3, 0.5, 0.7, and 0.9 respectively.

Subsystems with $q_S > 0.75$ can be detected by double lines independently of the outer period. Several detections in this work belong to this category. However, doubling of the CCF is observable when the RV difference in the inner subsystem exceeds a few km s^{-1} , in which case the single-measurement strategy also works. For simplicity, I do not account for this additional detection channel in the statistical analysis of the next Section.

4. STATISTICS OF SUBSYSTEMS IN WIDE BINARIES

The list of wide binaries in the FG-67 sample was created using the following criteria: separation larger than

8", V magnitudes of the secondary from 8 to 11, declination south of $+20^\circ$. The original list of 112 binaries was cleaned from optical systems and one white dwarf companion, leaving 98 wide binaries.

Table 4 concentrates relevant information on the selected binaries. Its column (1) is the *Hipparcos* number of the primary component and designations of the wide-binary components. Columns (2) to (5) give the parallax (mostly from van Leeuwen 2007), the visual magnitudes of both components, and the separation, respectively. Column (6) contains the characteristic amplitude of the orbital motion in the wide binary A^* computed from the projected separation and masses of the components given in FG67a. Then in columns (8) and (9) the average RVs of the primary and secondary components are given, while Column (9) gives reference codes for these RVs, explained in the notes to the table. When only one code is given, it covers both components. In two cases I found only low-accuracy RVs in SIMBAD. If there are several RV sources, I gave preference to this work and/or selected the same source for both components where available. The average RVs of spectroscopic subsystems are replaced by 'S2' or S1'. The presence of subsystems in the primary and secondary components of each binary is indicated in Columns (10) and (11), respectively, using the codes of FG67a. Briefly, 'C' means subsystems wider than $\sim 3''$, 'V' and 'v' stand for close resolved subsystems, 's2' and 'S2' mean double-lined spectroscopic binaries, 's' and 'S1' mean single-lined binaries, 'a' stands for acceleration binaries. A plus sign indicates sub-subsystems (spectroscopic pair in the close visual binary HIP 64478A). The last Column (10) gives *Hipparcos* or other identifications of secondary components, where available.

Not all subsystems are absolutely certain, e.g. the spectroscopic subsystems in both components of HIP 36165 announced in the GCS. I do not include the potential subsystem in HIP 14519 discovered by the ΔV method. The apparently non-hierarchical system HIP 22611 is removed from the following analysis, leaving 96 wide pairs.

Subsystems are found in 43 pairs, 25 of which have subsystems in the primary component, 28 in the secondary, and 10 in both ($43 = 25 + 28 - 10$). Obviously, the frequency of subsystems in the primary and secondary components is statistically the same. This sample gives a weak evidence of the correlated occurrence of subsystems in both components, noted previously in (Riddle et al. 2015) and FG67b. If the occurrence of subsystems were statistically independent, the expected number of wide binaries with subsystems in both components would be $96 \times (25/96) \times (28/96) = 7.3$, slightly less than the actual number 10.

Figure 5 compares periods and mass ratios of subsystems in the secondary components with their detection probability. The probability is calculated by the prescription of FG67a. The additional factor from ΔV measurements is incorporated for the 53 binaries without subsystems. The four subsystems with unknown periods and mass ratios are depicted by crosses located arbitrarily. The addition of spectroscopic coverage has dramatically improved the detection at $P < 10^4$ days in comparison with imaging-only surveys such as (Tokovinin 2014c). Such plot for the primary subsystems is simi-

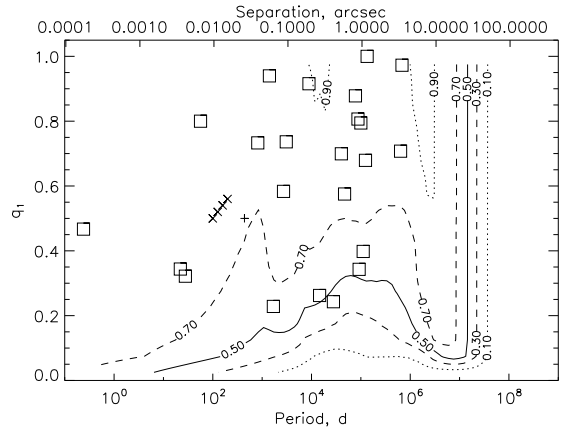


Figure 5. Secondary subsystems in the (P, q) space (squares). Crosses denote unknown periods and mass ratios, placed arbitrarily. The contours show average detection probability. The upper axis gives approximate angular separation at a distance of 50 pc. lar, with slightly deeper detection contours.

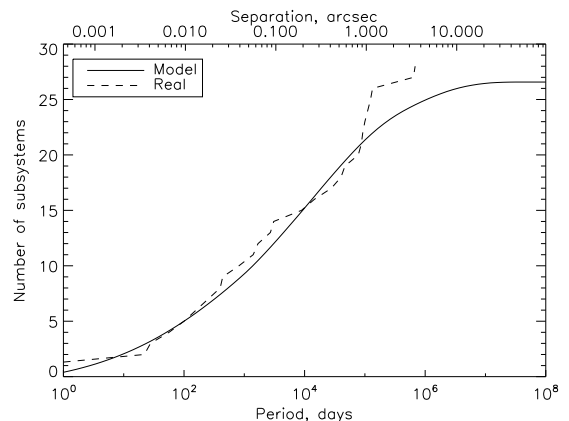


Figure 6. Cumulative distribution of periods in secondary subsystems (dashed line) and its model for $\beta = 1$ (full line).

It is instructive to compare the frequency and periods of subsystems with the statistical model developed in FG67b. The basic assumption is that subsystems are chosen randomly from the log-normal distribution of periods, keeping only dynamically stable multiples. I adopted the following parameters of the underlying period distribution: $x_0 = 4.54$, $\sigma = 2.40$, the mass-ratio exponent $\beta = 1$, and the total binary frequency $\epsilon = 0.5$ (see FG67b for description of those parameters). Two-dimensional distribution in the (P, q) space was multiplied by the detection probability and the dynamical truncation, providing the expected period distribution in the subsystems and their total number. It is compared to the actual cumulative distribution of secondary periods in Figure 6. The four yet unknown periods were given arbitrary values close to 100 days. The model predicts 26.6 secondary subsystems for $\beta = 1$ and 23.1 for $\beta = 0$, while the actual number is 28. This calculation was repeated for the primary subsystems, giving their predicted numbers of 32.4 and 29.1 for $\beta = 1$ and $\beta = 0$, respectively; the actual number is 25. The numbers match within statistical errors, as do the period distributions (with the caveat related to unknown periods). Therefore, the data collected here support the statistical description of multiplicity proposed in FG67b.

5. ECCENTRICITIES OF WIDE BINARIES

In this Section, I study the distribution of the observed RV difference in 53 wide binaries without known subsystems. The cumulative distribution of the normalized quantity $|\Delta V|/A^*$ is plotted in Figure 7 and compared to the simulated distributions presented in Figure 3. A good agreement with the case-3 simulation (uniformly distributed eccentricity) and a poor match with the “thermal” eccentricity distribution are obvious. The observed distribution is widened by the RV errors (both random and systematic) and by yet undetected subsystems. So, the real distribution should be even narrower than the observed one. This means that the eccentricities of wide binaries are likely even smaller than in the case 3.

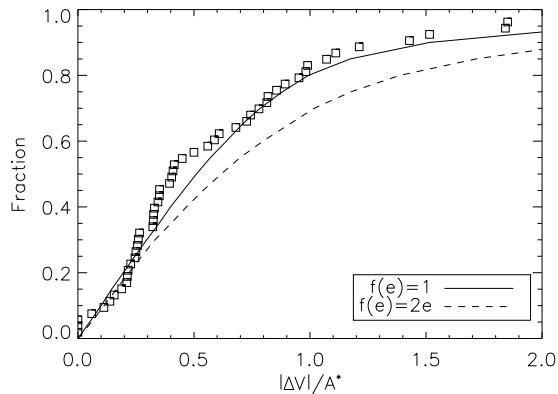


Figure 7. Cumulative distribution of the normalized RV difference in 53 wide binaries without subsystems (squares) is compared to simulations for uniformly distributed outer eccentricities (full line) and for the linear outer eccentricity distribution (dashed line).

Reipurth & Mikkola (2012) suggested that very wide binaries can form through ejection of one star from compact triple systems. Outer orbits of such ejected stars mostly have large eccentricities with typical values of ~ 0.7 (see their Figure 2). The wide binaries studied here have separations on the order of 10^3 AU, as in the above paper. However, eccentricities of those binaries without subsystems appear to be moderate, as follows from the RV differences between their components. Moreover, the frequency of subsystems in the primary and secondary components is similar, which speaks against the ejection scenario. Interestingly, Raghavan et al. (2010) found that eccentricities of binaries in the 25-pc volume are distributed approximately uniformly independently of their period. However, they based this conclusion on known spectroscopic and visual orbits which do not include binaries as wide as studied here.

6. SUMMARY

Results of the RV survey of nearby stars are reported. I focused on wide visual binaries and aimed at detecting subsystems in their components by a presence of double lines or by a substantial RV difference between the components. This latter “snapshot” technique is studied by simulation, showing that the major factor limiting the subsystem detection is the orbital motion in the wide binary itself. The survey readily detects subsystems with short periods. Non-detections are interpreted statistically, constraining the parameters of subsystems

and their overall frequency.

As most of the primary components of wide binaries in this sample already have RV coverage in the literature, I observed fainter and less-well studied secondaries. Five new subsystems in wide binaries were discovered in this project. The frequency of subsystems in the primary and secondary components turns out to be statistically the same. The data match the crude model proposed in FG67b, where subsystems are chosen randomly from the general period distribution and are constrained only by dynamical stability.

An interesting additional result concerns wide binaries without subsystems. The distribution of the observed RV difference between their components places some constraints on the distribution of the orbital eccentricities, which are not measured directly owing to very long periods. The results of this work rule out the “thermal” distribution $f(e) = 2e$ and match instead the uniform distribution. This suggests that dynamical interactions in N -body stellar systems were not dominant in shaping the orbits of wide binaries.

I thank the operators of the 1.5-m telescope for executing observations of this program and the SMARTS team at Yale for scheduling and pipeline processing. This work used the SIMBAD service operated by Centre des Données Stellaires (Strasbourg, France), bibliographic references from the Astrophysics Data System maintained by SAO/NASA, and the Washington Double Star Catalog maintained at USNO.

Facilities: CTIO:1.5m.

REFERENCES

- Bate, M. R. 2012, MNRAS, 419, 3115.
 Chubak, C. & Marcy, G. 2011, BAAS, 43,
 Desidera, S., Gratton, R., Lucatello, S. et al. 2006, A&A, 454, 553
 Duchêne, G. & Kraus, A. 2013, ARAA, 51 (ArXiv:1303:3028)
 Griffin, R. F. 2001, Obs, 121, 221
 Halbwachs, J.-L., Mayor, M., & Udry, S. 2012, MNRAS, 422, 14
 Latham, D. W., Stefanik, R. P., Torres, G., & Davis, R. J. 2002
 AJ, 124, 1144
 Nidever, D. L., Marcy, G. W., Butler, R. P. et al. 2002, ApJS,
 141, 503
 Nordström, B., Mayor, M., Andersen, J. et al. 2004, A&A, 418,
 989 (GCS)
 Pourbaix, D., Tokovinin, A. A., Batten, A. H. et al. 2004 A&A,
 424, 727 (SB9)
 Raghavan, D., McAlister, H. A., Henry, T. J. et al. 2010, ApJS,
 190, 1
 Reipurth, Bo, & Mikkola, S. 2012, Nature, 492, 221
 Riddle, R. L., Tokovinin, A., Mason, B. D. et al. 2015, ApJ, 799, 4
 Saar, S. H., Nordström, B., & Andersen, J. 1990, A&A, 235, 291
 Sahlmann, J., Ségransan, D., Queloz, D. et al. 2011, A&A, 525, 95
 Tokovinin, A. & Smekhov, M. G. 2002, A&A, 382, 118
 Tokovinin, A., Thomas, S., Sterzik, M., & Udry, S. 2006, A&A,
 450, 681
 Tokovinin, A., Fischer, D. A., Bonati, M. et al. 2013, PASP, 125,
 1336
 Tokovinin, A. AJ, 2014a, 147, 86 (FG67a)
 Tokovinin, A. AJ, 2014b, 147, 87 (FG67b)
 Tokovinin, A. 2014c, AJ, 148, 72
 Tokovinin, A., Pribulla, T., & Fischer, D. 2015a, AJ, 149, 8
 Tokovinin, A., Mason, B. D., Hartkopf, W. I. et al. 2015b, AJ,
 150, 50
 Torres, C. A. O., Quast, G. R., Da Silva, L. et al. 2006, A&A,
 460, 695
 van Leeuwen, F. 2007, A&A, 474, 653 (HIP2)

Table 4
Subsystems in wide binaries

HIP, Comp.	π_{HIP} (mas)	V_1 (mag)	V_2 (mag)	Sep. (")	A^* (km s ⁻¹)	RV1 (km s ⁻¹)	RV2 (km s ⁻¹)	Reference	Sys1	Sys2	Comment
2292 A,B	17.6	7.9	9.4	839.3	0.2	9.6	9.6	GCS,L02	...	v	B=2350
2888 A,B	22.9	6.8	8.5	329.8	0.5	S2	S1	SB9,T06	S2	S1	B=2848
3203 A,B	37.7	7.0	9.9	8.5	2.6	12.0	n/a	N04,CfA	
3795 AB,C	15.6	7.7	10.8	152.3	0.6	-21.40	n/a	GCS	V	v	
6772 A,B	16.6	8.2	11.1	389.1	0.3	49.9	50.4	CHI	B=6804
9902 A,B	22.6	7.6	10.5	52.2	0.9	11.5	11.0	CHI	
9911 A,B	27.1	7.0	10.5	79.2	0.8	-39.1	-38.7	CHI	
11024 A,B	24.4	8.0	10.4	10.3	1.9	45.2	45.2	CHI	
11137 A,B	17.0	8.9	9.4	34.7	0.9	26.3	26.6	L02	B=11134
11783 A,B	37.5	4.8	8.8	345.3	0.5	-24.6	-28.3	CHI	s,a,v	...	B=11759
12780 A,B	24.2	7.0	8.5	12.5	2.4	S2	S1	CHI	V,S2	S1	
14194 A,B	18.8	7.6	10.0	8.7	2.2	35.3	s2	CHI	...	s2	
14307 A,B	18.7	7.6	8.6	38.3	1.1	20.4	s2	GCS,CHI	...	v,s2	B=14313
14519 A,B	18.8	9.1	10.6	60.3	0.7	15.9	17.7	CHI	...	s1?	
15527 A,B	28.1	7.4	8.5	253.0	0.4	39.5	39.6	GCS	B=15526
16860 A,B	21.1	9.0	10.9	31.5	1.0	-26.1	-24.9	GCS,CHI	B=16858
18888 A,B	15.9	8.2	8.6	595.2	0.3	33.7	33.7	GCS	...	v	B=18958
21923 A,B	23.0	7.2	10.2	141.6	0.6	14.5	S2	SIM,H12	...	S2	B=21946
22611 A,C	16.9	6.7	8.7	51.9	0.9	45.7	46.4	CHI	
22611 A,B	16.9	6.8	9.0	99.6	0.7	45.7	46.0	CHI	B=22604
22826 A,B	19.9	7.2	8.7	415.9	0.3	12.1	12.0	GCS	B=HD 31222
23693 A,B	85.9	4.8	9.0	321.7	0.6	-0.8	-0.7	GCS,CHI	B=23708
23926 A,B	18.7	6.8	10.3	10.1	1.9	43.8	45.1	GCS,CHI	B=23923
24711 A,B	15.3	8.5	10.6	13.4	1.5	-11.3	-10.8	GCS,CHI	v	...	B=24712
25082 A,B	17.6	7.1	10.1	9.5	1.9	25.1	23.2	GCS,CHI	
27922 A,B	42.4	7.6	10.6	10.6	2.3	42.1	44.0	GCS,CHI	
31711 AB,C	47.0	6.3	9.8	808.6	0.4	28.1	31.6	GCS,CHI	V,s,a	...	C=31878
33705 A,B	26.8	6.7	8.6	323.9	0.4	16.3	16.4	GCS	B=33691
34065 AB,C	60.5	5.6	8.8	184.9	0.9	88.1	S1	GCS,S11	C	a,S1,v	C=34052
34065 A,B	60.5	5.6	7.0	21.0	2.7	88.1	88.0	GCS	B=34069
36165 A,B	31.2	7.1	8.1	17.7	1.8	66.7	66.3	GCS	s	s	B=36160
36485 AB,D	22.0	7.4	8.0	112.0	0.8	-1.0	S1	GCS,H12	C	S1,a,v	D=36497
36640 A,B	35.8	6.0	8.7	23.4	1.7	54.8	56.3	GCS,CHI	B=36642
37645 A,B	19.6	7.1	10.4	9.6	2.3	S1	-16.4	CfA,CHI	S1,v	...	
38908 A,BC	61.7	5.6	9.9	60.6	1.3	14.7	17.0	GCS,CHI	...	v	
40452 A,B	25.9	7.7	9.8	32.0	1.1	20.5	21.2	GCS,CHI	
42488 A,B	27.5	7.3	8.6	25.9	1.4	-20.3	-20.2	GCS,C11	s	...	B=42491
44579 A,B	15.5	8.7	9.3	140.5	0.4	2.2	0.6	GCS,CHI	B=HD 77759
45734 A,B	17.6	8.4	9.7	9.0	2.5	s2	s2	CHI	v,s	s2	
45838 C,AB	16.5	7.5	9.2	135.0	0.6	52.6	55.0	GCS,CHI	...	V	AB=HD 60815
46236 A,B	21.4	7.0	10.2	19.3	1.4	30.2	31.0	GCS,CHI	
47058 A,B	21.3	7.9	10.5	8.1	2.1	60.0	S1	GCS,CfA	...	S1	
47839 A,B	19.0	8.1	8.2	18.8	1.8	-2.2	-2.4	GCS	B=47836
47862 A,B	15.8	7.2	10.8	9.6	1.8	-16.5	-14.5	GCS,CHI	
48785 A,B	23.9	7.7	8.4	30.6	1.2	30.4	31.0	GCS	B=48786
49030 A,B	16.7	7.7	10.5	24.2	1.1	14.7	15.8	GCS,CHI	
49520 A,B	16.9	8.8	9.0	9.5	1.9	-0.4	0.3	D06	...	v	
56242 A,B	42.9	6.4	9.2	15.5	2.1	-4.9	-4.9	GCS	
57148 A,BC	16.0	8.4	9.8	24.9	1.2	4.3	4.3	LCO	...	v	BC=57146
58067 A,B	24.7	8.3	8.5	73.4	0.8	5.9	5.6	GCS	B=58703
58813 A,B	18.3	8.1	8.8	23.2	1.2	6.0	5.5	GCS	B=58815
59272 A,B	45.0	7.0	9.7	9.4	2.7	1.6	2.7	GCS,CHI	
59690 A,B	18.1	7.6	9.7	23.2	1.2	24.2	25.1	GCS,CHI	B=59687
60353 A,B	33.4	6.6	10.5	20.7	1.7	4.3	4.4	GCS,CHI	B=60352
60749 AB,D	15.9	8.5	10.2	24.7	1.3	-3.9	-1.8	GCS,CHI	V	...	D=60750
61595 A,B	17.8	8.3	10.9	8.4	1.9	-13.7	-15.3	GCS,CHI	
64478 A,B	23.7	6.3	9.4	25.1	1.9	S2	S2	S90,CHI	V+S2	S2	
64498 A,B	18.0	7.6	9.9	9.3	2.2	-12.0	-15.7	CHI	v	...	
66121 A,B	28.4	6.5	9.3	22.1	1.5	-28.9	-28.4	GCS,CHI	B=66125
66676 A,BC	16.9	8.4	9.2	77.5	0.7	1.3	2.4	CHI	...	v	BC=HD 118735
67246 A,B	31.6	6.4	10.2	488.5	0.3	-30.9	-30.4	GCS,CHI	B=67291
67408 A,B	33.9	6.7	10.2	11.6	2.2	3.2	2.9	GCS,CHI	
69220 A,B	20.8	8.4	9.7	57.5	0.8	48.9	50.0	GCS,CHI	B=69224
71682 A,CD	23.4	7.1	10.0	123.0	0.7	11.1	13.2	GCS,CHI	a	v	CD=71686
72235 A,B	24.0	8.6	10.8	9.1	2.1	9.1	9.1	CHI	...	v	
74930 A,B	20.0	7.2	8.1	13.3	1.8	-35.9	-36.7	GCS	B=74931
74975 A,B	39.4	5.1	10.1	11.4	2.6	54.2	55.1	GCS,CHI	
75790 AB,C	17.1	7.0	10.1	9.6	2.3	-12.2	-10.9	LCO	v	...	
76435 A,C	20.6	9.1	10.6	13.5	1.8	5.4	7.3	CHI	...	v	
76888 A,B	15.0	9.3	9.4	23.2	1.1	8.1	7.9	CHI	B=76891
78738 A,B	39.6	7.5	8.1	11.8	2.3	-31.8	-32.3	GCS	B=78739
79730 A,B	21.1	7.2	8.7	19.8	1.4	-40.6	-40.1	GCS,CHI	
83701 A,B	17.1	7.9	10.0	97.2	0.6	-1.3	-1.1	GCS,CHI	
85342 A,B	21.1	7.0	8.9	127.2	0.6	-15.9	-16.6	GCS	...	a,s,v	B=85326

Table 4 — *Continued*

HIP, Comp.	π_{HIP} (mas)	V_1 (mag)	V_2 (mag)	Sep. ($''$)	A^* (km s^{-1})	RV1 (km s^{-1})	RV2 (km s^{-1})	Reference	Sys1	Sys2	Comment
90355 A,B	27.3	7.9	8.4	608.4	0.3	S1	-18.0	H12	A,S1	...	B=90365
91837 AB,C	16.0	7.7	10.2	32.6	1.2	-4.2	-4.1	LCO	V	...	
93772 A,B	15.2	7.0	8.9	9.4	1.9	-18.2	-18.7	GCS,TS02	
95106 A,B	21.2	8.2	10.3	13.7	1.9	13.7	s1	GCS,FECH	v,s	s	B=95110
95116 A,B	15.9	7.1	9.3	8.8	2.0	-41.9	-41.1	CHI	
96979 A,B	15.1	6.9	8.7	27.3	1.1	-41.9	-41.6	GCS	B=96976
97508 AB,C	17.8	7.4	10.4	13.9	1.9	8.3	8.0	CHI	V	...	
99729 A,B	16.4	7.8	8.1	43.3	0.9	-0.9	-0.6	N02	B=99727
101551 A,B	16.7	7.9	9.6	10.4	1.7	21.4	21.4	CHI	B=101549
102418 A,CD	15.3	8.8	10.5	539.2	0.3	10.7	11.3	SIM,CHI	...	v	
102655 A,B	18.6	8.5	9.7	391.3	0.3	-2.6	-2.3	CHI	B=HD 198016
103311 AB,C	21.9	7.4	10.7	324.9	0.4	-4.5	-6.9	SACY	v	...	
105585 AB,C	18.0	8.9	9.0	18.1	1.6	s2	3.6	CHI	v,s2	...	C=105569
105879 A,D	15.8	7.3	10.0	44.0	0.9	s2	35.9	CHI	s2,a	...	
106438 A,B	20.4	7.8	9.8	40.3	0.9	-29.2	-29.0	CHI	
106632 A,B	16.5	8.8	10.0	11.4	1.6	16.7	16.3	CHI	B=106633
110447 A,B	15.0	9.1	10.2	12.6	1.4	1.4	2.5	CHI	B=110444
110712 A,B	43.4	6.1	8.9	20.6	2.1	14.6	15.3	FECH	...	v	B=110719
112201 A,B	18.5	8.3	9.8	179.0	0.4	-13.3	-12.9	GCS,CHI	
113386 A,B	16.3	7.6	9.2	9.1	1.9	0.5	0.9	CHI	
113579 A,B	32.5	7.6	9.7	581.2	0.3	7.0	s3	FECH	...	v	B=113597
114378 A,B	40.3	6.5	10.3	31.7	1.4	S1	-1.4	Griff01	S1	...	
114702 A,B	25.6	8.1	8.6	24.9	1.6	-30.0	S1	GCS,T06	...	v+S1	B=114703
116063 A,B	32.6	7.2	9.1	36.4	1.2	4.0	4.3	FECH	
117391 A,B	17.5	7.6	10.1	109.3	0.5	17.2	17.7	GCS,CHI	

References. — SIM: SIMBAD; C11: Chubak & Marcy (2011); CfA: D. Latham, 2012, private communication; CHI: this work, CHIRON data; D06: Desidera et al. (2006); FECH: this work, FECH data; GCS: Nordström et al. (2004); Griff01: Griffin (2001); H12: Halbwachs et al. (2012); L02: Latham et al. (2002); LCO: Tokovinin et al. (2015a); N02: Nidever et al. (2002); S11: Sahlmann et al. (2011); S90: Saar et al. (1990); SACY: Torres et al. (2006); SB9: Pourbaix et al. (2004); T06: Tokovinin et al. (2006); TS02: Tokovinin & Smekhov (2002).